

Autonomously stabilized entanglement between two superconducting quantum bits

S. Shankar¹, M. Hatridge¹, Z. Leghtas¹, K. M. Sliwa¹, A. Narla¹, U. Vool¹, S. M. Girvin¹, L. Frunzio¹, M. Mirrahimi^{1,2} & M. H. Devoret¹

Quantum error correction codes are designed to protect an arbitrary state of a multi-qubit register from decoherence-induced errors¹, but their implementation is an outstanding challenge in the development of large-scale quantum computers. The first step is to stabilize a non-equilibrium state of a simple quantum system, such as a quantum bit (qubit) or a cavity mode, in the presence of decoherence. This has recently been accomplished using measurement-based feedback schemes^{2–5}. The next step is to prepare and stabilize a state of a composite system^{6–8}. Here we demonstrate the stabilization of an entangled Bell state of a quantum register of two superconducting qubits for an arbitrary time. Our result is achieved using an autonomous feedback scheme that combines continuous drives along with a specifically engineered coupling between the two-qubit register and a dissipative reservoir. Similar autonomous feedback techniques have been used for qubit reset⁹, single-qubit state stabilization¹⁰, and the creation¹¹ and stabilization⁶ of states of multipartite quantum systems. Unlike conventional, measurement-based schemes, the autonomous approach uses engineered dissipation to counteract decoherence^{12–15}, obviating the need for a complicated external feedback loop to correct errors. Instead, the feedback loop is built into the Hamiltonian such that the steady state of the system in the presence of drives and dissipation is a Bell state, an essential building block for quantum information processing. Such autonomous schemes, which are broadly applicable to a variety of physical systems, as demonstrated by the accompanying paper on trapped ion qubits¹⁶, will be an essential tool for the implementation of quantum error correction.

Here we implement a proposal¹⁷, tailored to the circuit quantum electrodynamics (cQED) architecture¹⁸, for stabilizing entanglement between two superconducting transmon qubits¹⁹. Each transmon consists of a Josephson junction capacitively shunted to form an anharmonic oscillator whose lowest two levels are used as the qubit. The qubits are dispersively coupled to an open cavity that acts as the dissipative reservoir. The cavity in our implementation is furthermore engineered to decay preferentially into a 50-Ω transmission line that we monitor on demand. We show, using two-qubit quantum state tomography and high-fidelity single-shot readout, that the steady state of the system reaches the target Bell state with a fidelity of 67%, which is well above the 50% threshold that signifies entanglement. The fidelity can be further improved by monitoring the cavity output and performing conditional tomography when the output indicates that the two qubits are in the Bell state¹⁷. We implemented this protocol by means of post-selection and demonstrated that the fidelity increased to ~77%.

Our cQED set-up (Fig. 1a) consists of two individually addressable qubits, Alice and Bob, coupled dispersively to a three-dimensional (3D) rectangular copper cavity. The set-up is described by the dispersive Hamiltonian²⁰

$$\begin{aligned} \frac{H}{\hbar} = & \omega_A^0 a^\dagger a + \omega_B^0 b^\dagger b + \omega_c^{gg} c^\dagger c - \frac{1}{2} \alpha_A (a^\dagger a)^2 \\ & - \frac{1}{2} \alpha_B (b^\dagger b)^2 - \chi_A a^\dagger a c^\dagger c - \chi_B b^\dagger b c^\dagger c \end{aligned} \quad (1)$$

Here a , b and c are respectively the annihilation operators of the Alice and Bob qubits and the cavity mode; a^\dagger , b^\dagger and c^\dagger are the corresponding creation operators; ω_A^0 and ω_B^0 are the Alice and Bob qubit angular frequencies when there are no photons in the cavity; ω_c^{gg} is the cavity frequency when both qubits are in the ground state (see Methods for experiment parameters); α_A and α_B are respectively the Alice and Bob

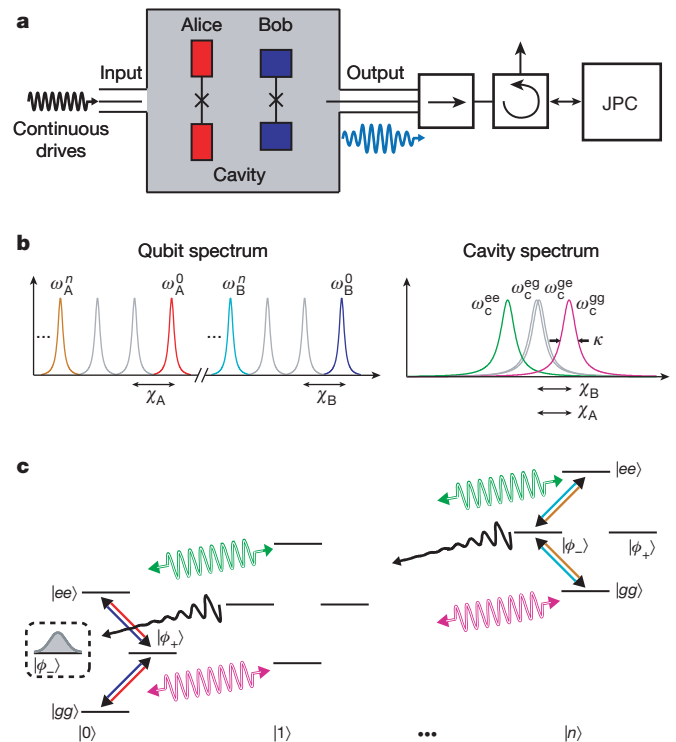


Figure 1 | Bell state stabilization set-up schematic and frequency landscape of autonomous feedback loop. **a**, The qubits (Alice and Bob) are coupled to the fundamental mode of a 3D cavity. Six continuous drives applied to the cavity input stabilize the Bell state $|\phi_-, 0\rangle$. The cavity output jumps between low and high amplitude depending on whether the qubits are in the desired Bell state or not. The output is monitored by a quantum-limited amplifier (JPC). **b**, Spectra of the qubits and cavity coupled with nearly equal dispersive shifts (χ_A and χ_B); κ is the cavity linewidth. Colours denote transitions that are driven to establish the autonomous feedback loop. **c**, Effective states of the system involved in the feedback loop. Qubit states consist of the odd-parity states in the Bell basis $\{|\phi_-\rangle, |\phi_+\rangle\}$ and the even-parity computational states $\{|gg\rangle, |ee\rangle\}$. Cavity states, arrayed horizontally, are the photon-number basis kets $|n\rangle$. Sinusoidal double lines represent the two cavity tones whose amplitudes create on average \bar{n} photons in the cavity when the qubits are in even-parity states. The cavity level populations are Poisson distributed with mean \bar{n} and we show only $|n\rangle$ such that $n \approx \bar{n}$. Straight double lines represent four tones on qubit transitions. Collectively, the six tones and the cavity decay (decaying sinusoidal lines) drive the system towards the 'dark' state, $|\phi_-, 0\rangle$, which builds up a steady-state population.

¹Department of Applied Physics and Physics, Yale University, New Haven, Connecticut 06520, USA. ²INRIA Paris-Rocquencourt, Domaine de Voluceau, BP 105, 78153 Le Chesnay Cedex, France.

qubit anharmonicities; and χ_A and χ_B are the respective dispersive couplings, which are designed to be nearly equal. The cavity linewidth, κ , and the qubit decoherence rates, $\Gamma_1^{A,B}$ and $\Gamma_\phi^{A,B}$, are smaller than χ_A and χ_B , such that the system operates in the strong-dispersive limit of cQED²¹, where ω_A^n and ω_B^n , the qubit transition frequencies for different cavity photon occupancies, n , are clearly resolved. As described in Fig. 1b, by applying six continuous drives, four at qubit transitions and two at cavity transitions, an effective feedback loop is established that forces the two qubits into the Bell state $|\phi_-\rangle \equiv (|ge\rangle - |eg\rangle)/\sqrt{2}$ with zero photons in the cavity.

The feedback loop shown in Fig. 1c can be broken down into two parts that operate continuously and concurrently: the first is equivalent to a measurement process, and the second is equivalent to qubit rotations conditioned on the measurement outcome. The measurement process, implemented by two drives at the cavity frequencies, ω_c^{gg} and ω_c^{ee} , together with the approximately equal dispersive shifts, distinguishes the even-parity manifold, where the qubits are parallel, from the odd-parity manifold, where they are antiparallel. The odd-parity manifold is conveniently described in the Bell basis $\{|\phi_-\rangle, |\phi_+\rangle\}$, which contains our target state, $|\phi_-\rangle$. The drives, together with cavity dissipation, can be regarded as implementing a continuous projective measurement of the state of the two qubits that leaves the odd-parity manifold unaffected^{22,23}. The drives are resonant when the qubits are in $|gg\rangle$ or $|ee\rangle$, such that an average of \bar{n} photons at ω_c^{gg} or ω_c^{ee} continuously traverse the cavity every lifetime, $1/\kappa$. However, when the qubits have odd parity, both drives are far off-resonance because $\chi_A, \chi_B \gg \kappa$, thus leaving the cavity almost empty of photons. As a result, the average number of photons in the cavity, the pointer variable ‘observed’ by the environment¹, projects the even-parity manifold into $|gg\rangle$ and $|ee\rangle$, and distinguishes them from the odd-parity manifold, which is left unperturbed.

The second part of the feedback loop uses the photon-number splitting (quantized light shifts) of the qubit transitions in the strong-dispersive limit to implement conditional qubit rotations. Two drives are applied selectively at the zero-photon qubit frequencies, ω_A^0 and ω_B^0 , with amplitudes set to give equal Rabi frequencies of $\Omega^0 \approx \kappa \ll \chi_A, \chi_B$. The phases of these drives set, by definition, the x axis of each qubit’s Bloch sphere. The action of these drives is described by the effective unitary rotation operator $(a + a^\dagger) \otimes I^B + I^A \otimes (b + b^\dagger)$ on the two qubit subspace, where I^A and I^B are the respective identity matrices. Therefore, they rotate the undesired Bell state, $|\phi_+, 0\rangle$, into the even-parity manifold, leaving the desired one, $|\phi_-, 0\rangle$, untouched. Thus, any population in $|\phi_+, 0\rangle$ is eventually pumped out by the combined action of the zero-photon qubit drives and the cavity drives.

To re-pump population into the target Bell state, $|\phi_-, 0\rangle$, two more drives with equal Rabi frequencies, Ω^n , are applied at $\omega_A^0 - n(\chi_A + \chi_B)/2$ and $\omega_B^0 - n(\chi_A + \chi_B)/2$, which are near the n -photon qubit frequencies, ω_A^n and ω_B^n , shown in Fig. 1b. The phase of the drive on Alice is set to be along the x axis of its Bloch sphere, whereas that on Bob is set to be antiparallel to its x axis, resulting in the effective unitary rotation operator $(a + a^\dagger) \otimes I^B - I^A \otimes (b + b^\dagger)$ (see Methods for details on the phase control of qubit drives). Thus, as long as $n \approx \bar{n}$, these two drives shuffle population from $|gg, n\rangle$ and $|ee, n\rangle$ into the state $|\phi_-, n\rangle$. The latter state is unaffected by the cavity drives and therefore decays irreversibly, at a rate κ , to the desired target Bell state, $|\phi_-, 0\rangle$.

Thus, when all six drives are turned on, the continuously operating feedback loop forces the two qubits into $|\phi_-\rangle$ even in the presence of error-inducing relaxation ($\Gamma_1^{A,B}$) and dephasing ($\Gamma_\phi^{A,B}$) processes. As shown in Extended Data Fig. 4, simulations indicate that the drive amplitudes should be optimally set to give Rabi frequencies $\Omega^0 \approx \Omega^n \approx \kappa/2$ and $\bar{n} \approx 3-4$. For these parameters, the two qubits are expected to stabilize into the target state at a rate of order $\kappa/10$, which can be understood from the successive combination of transition rates, each of which is of order κ . With the experimental parameters in our implementation, the feedback loop is expected to correct errors and stabilize the two qubits into $|\phi_-\rangle$ with a time constant of about 1 μ s.

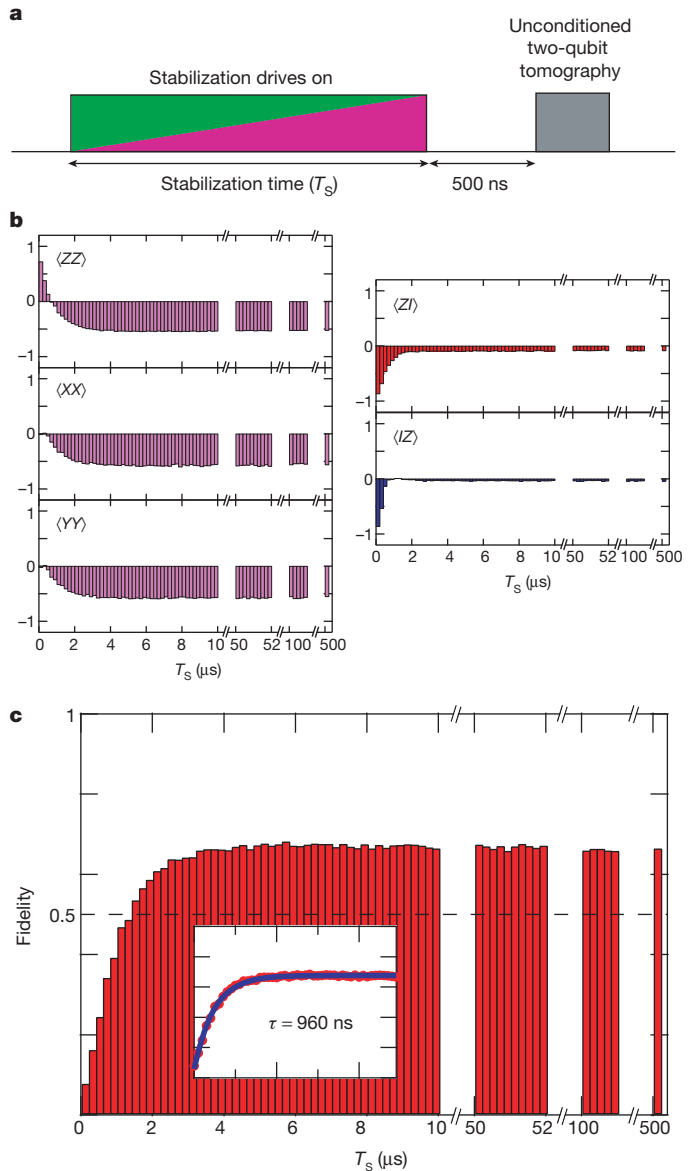


Figure 2 | Convergence of two qubit-state to the target Bell state. **a**, The six drives are turned on during the stabilization period for time T_s . Next, the drives are turned off and the system is left idle for 500 ns, allowing any remaining cavity photons to decay away. Finally, two-qubit tomography is performed using single-qubit rotations followed by single-shot joint readout. The system is then allowed to reach thermal equilibrium by waiting at least $5T_1$ before repetition. **b**, Time variation of the relevant Pauli operator averages, showing the system’s evolution from thermal equilibrium (nearly $|gg\rangle$) towards $|\phi_-\rangle$. The system remains in this steady state for an arbitrarily long time, as demonstrated by data acquired at $T_s = 50, 100$ and 500μ s. **c**, Fidelity to the target state $|\phi_-\rangle$ as a function of stabilization time, T_s . The dashed line at 50% is the entanglement threshold. The fidelity converges to 67% with a time constant, τ , of about ten cavity lifetimes, in good agreement with the theoretical prediction; inset, F for $T_s = 0-10 \mu$ s (red circles), with exponential fit (blue line).

The fidelity of the stabilized state to $|\phi_-\rangle$ is determined by the competition between the correction rate, $\kappa/10$, and the rates, $\Gamma_1^{A,B} = 1/T_1^{A,B}$ and $\Gamma_\phi^{A,B} = 1/T_\phi^{A,B}$, at which the Alice–Bob system decoheres out of the target state. Thus, to achieve a high-fidelity entangled state, the system–reservoir parameters χ_A, χ_B and κ have to be engineered such that $\chi_A = \chi_B > \kappa$, while maintaining $\kappa \gg \Gamma = \max(\Gamma_1^{A,B}, \Gamma_\phi^{A,B})$. In the present experiment, we built on recent advances in the coherence of superconducting qubits achieved by using 3D cavities²⁴ to obtain $\chi/\kappa \approx 4$ and $\kappa/\Gamma \approx 100$ simultaneously, satisfying both requirements.

The protocol of the experiment consists of applying the six continuous drives for a length of time T_S (Fig. 2a) and verifying the presence of entanglement by performing two-qubit state tomography. State tomography is realized by applying one of a set of 16 single-qubit rotations and then performing joint qubit readout²⁵, implemented here using single-shot measurements. As described in Fig. 1a, Extended Data Fig. 1 and Methods, the dispersive joint two-qubit readout is implemented by pulsing the cavity at ω_c^{gg} and recording the cavity output for 240 ns using a nearly quantum-limited microwave amplification chain. The first amplifier in the chain is a Josephson parametric converter (JPC) operated as a phase-preserving amplifier²⁶, which performs single-shot projective readout of the state of the two qubits with a fidelity of more than 96% in our experiment (Extended Data Fig. 2 and Methods). The averages of the 16 two-qubit Pauli operators $\langle AB \rangle$, where A and B are each one of the four single-qubit operators $\{I, X, Y, Z\}$ for Alice and Bob, respectively, are calculated by repeating the tomography 5×10^5 times per operator, resulting in a statistical imprecision of about 0.2%.

Tomography results as a function of the duration of the stabilization interval, T_S , are illustrated in Fig. 2b, showing the expected convergence of the system to the Bell state $|\phi_{-}\rangle$. For $T_S = 0$, the Pauli operator averages are $\langle ZI \rangle = \langle IZ \rangle = 0.86$ and $\langle ZZ \rangle = 0.72$, indicating that the system is mostly in $|gg\rangle$ when no drives are present. With increasing T_S , the single-qubit averages tend to zero, whereas the two-qubit averages $\langle ZZ \rangle$, $\langle XX \rangle$ and $\langle YY \rangle$ stabilize at negative values, whose sign is characteristic of $|\phi_{-}\rangle$. The autonomous feedback loop operation was verified with snapshots taken for values of T_S up to 500 μ s, indicating that the steady state of the two qubits remains stable for times well in excess of the timescales of decoherence processes.

The fidelity, F , of the measured state to the target, $|\phi_{-}\rangle$, is $F = \text{Tr}(\rho_{\text{target}}\rho_{\text{meas}})$, where $\rho_{\text{target}} = |\phi_{-}\rangle\langle\phi_{-}|$ and ρ_{meas} is obtained from the measured set of two-qubit Pauli operators. As shown in Fig. 2c, F stabilizes at 67%, which is well above the threshold of 50% that indicates the presence of entanglement. Entanglement is also evidenced by the non-zero concurrence²⁷, $C = 0.36$. The exponential rise of F with a time constant of 960 ns (Fig. 2c, inset), or approximately ten cavity lifetimes, is in good agreement with the expected 1- μ s correction time constant of the autonomous feedback loop.

As expected, the steady state reached by the autonomous feedback loop is impure. By analysing the density matrix constructed from tomography, we calculate that it contains 67% weight in $|\phi_{-}\rangle\langle\phi_{-}|$ and that the weights in the undesired states $|gg\rangle\langle gg|$, $|ee\rangle\langle ee|$ and $|\phi_{+}\rangle\langle\phi_{+}|$ are 15%, 10% and 8%, respectively. However, the reservoir (cavity output) contains information on the qubits' parity that can be exploited. Thus, the state fidelity can be conditionally enhanced by passively monitoring this output and performing tomography only when the loop indicates that the qubits are in an odd-parity state (eliminating weights in the even-parity states $|gg\rangle\langle gg|$ and $|ee\rangle\langle ee|$). A version of this protocol (Fig. 3) is implemented in essence by passively recording the cavity output at ω_c^{gg} for the last 240 ns of the stabilization period (measurement M_1 in Fig. 3a). A reference histogram for M_1 (Fig. 3b) shows Gaussian distributions separated by two standard deviations, allowing us to remove any $|gg\rangle\langle gg|$ component present in the ensemble at the end of the stabilization period, by applying an exclusionary threshold, I_m^{th}/σ . We again perform single-shot tomography (measurement M_2 in Fig. 3a) after 100 ns and post-select M_2 for trials where M_1 indicates that the qubits are not in the state $|gg\rangle\langle gg|$ ($M_1 = \overline{GG}$), in the process keeping $\sim 1\%$ of counts. This conditioned tomography improves F to 77% ($C = 0.54$), in good agreement with a simple estimate of $67/(67 + 10 + 8) = 79\%$ when the weight of $|gg\rangle\langle gg|$ is removed. Additionally monitoring the cavity output at ω_c^{ee} could straightforwardly improve the conditioned fidelity to 90%, and would be achievable through modest improvements of the Josephson amplifier bandwidth. Thus, in addition to fully autonomous Bell state stabilization, we have demonstrated that, in principle, real-time electronics monitoring can significantly increase the Bell state purity.

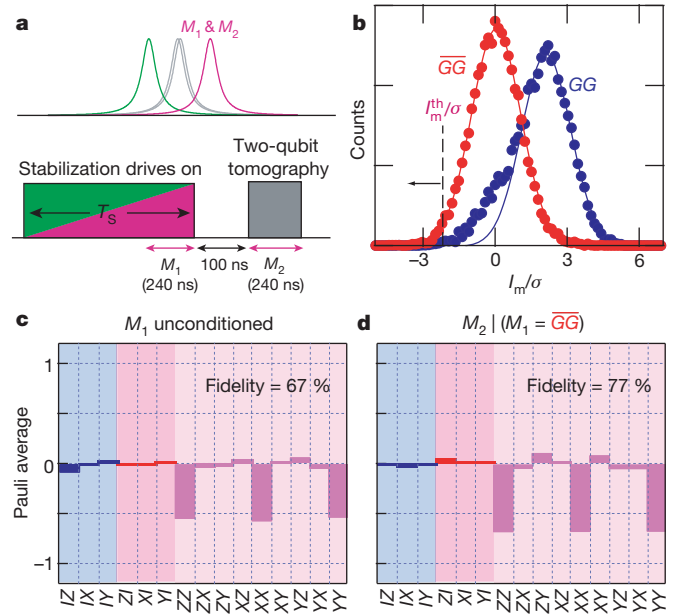


Figure 3 | Fidelity improved by monitoring the feedback loop. **a**, Pulse sequence consisting of a $T_S = 10$ - μ s period followed by two-qubit tomography. Here, the cavity output at ω_c^{gg} is recorded during the last 240 ns of the stabilization period (M_1). The outcomes obtained during M_1 are used to condition the tomography in post-processing. After waiting 100 ns for any cavity photons to decay away, two-qubit state tomography is performed using a second 240-ns-long measurement (M_2) similar to that used in the unconditioned tomography (Fig. 2). **b**, Reference histogram for M_1 , with qubits prepared in thermal equilibrium (denoted GG) and after a π -pulse on Alice (denoted \overline{GG}). The standard deviation, σ , of the Gaussian distributions scales the horizontal axis of measurement outcomes, I_m . **c**, Complete set of Pauli operator averages measured by tomography without conditioning, as in Fig. 2, showing a fidelity of 67% to $|\phi_{-}\rangle$. **d**, Tomography conditioned on M_1 being \overline{GG} , that is, outcomes I_m/σ during $M_1 < I_m^{\text{th}}/\sigma = -2.2$, resulting in an increased fidelity of 77%.

We now address the basic imperfections of our experiment that limit the current value of the steady-state, unconditioned fidelity to 0.67. First, the fidelity measured by tomography is ~ 0.05 less than the theoretical steady-state value during the stabilization period, owing to the 500-ns wait time before tomography, during which the state decays under the influence of T_1 and T_ϕ . This wait period, which was introduced to ensure that the single-qubit rotations during tomography are not perturbed by residual cavity photons, can be reduced with conditioned tomography (to 100 ns; see Fig. 3a) because there will be fewer cavity photons when the qubits are in the target state. As shown in Methods, owing to this wait period the fidelity measured by tomography is not expected to be affected by extraneous systematic errors in calibration of single-qubit rotations (Extended Data Fig. 3). Furthermore, we also show that the fidelity is unaffected by the measurement infidelity of the readout. Instead, the sources of error are intrinsically determined by the environmental couplings inherent in the system and its coupling to the reservoir.

Although it might be supposed that mismatch between χ_A and χ_B would be a dominant cause for infidelity through measurement-induced dephasing²³, simulations (Methods) indicate that the present 10% mismatch contributes only 0.02 to the infidelity. This robust property of the feedback loop is achieved by setting the cavity drives on ω_c^{gg} and ω_c^{ee} transitions, which mitigate the measurement-induced dephasing, by comparison with the more straightforward irradiation between ω_c^{gg} and ω_c^{ee} proposed in usual parity measurement^{8,22,23}. The dominant mechanism for infidelity turns out to be the T_1 and T_ϕ processes, which contribute 0.12 and 0.08, respectively. The severity of these processes may actually be enhanced in the presence of cavity drives, which tend to shorten T_1 in transmon qubits²⁸. The remaining infidelity

can possibly be attributed to this shortening of T_1 , in combination with the presence of $|f\rangle$ (second excited state) population in each qubit due to finite qubit temperature. Overall, the dominant sources of infidelity (T_1 and T_ϕ) are likely to be mitigated in future experiments by expected improvements in qubit coherence (Methods), which will allow a larger ratio κ/Γ and, thus, fidelities in excess of 90%.

We have demonstrated the stabilization of two-qubit entanglement that makes a Bell state available for indefinite time, using a completely autonomous protocol. Although the fidelity to the Bell state does not presently exceed that needed for violation of Bell's inequality, straightforward improvements to the set-up should allow it¹⁷. In addition to sufficiently coherent qubits, the resources required, consisting of matching dispersive couplings and six pure tones sent through the same input line, are modest in comparison with the hardware that would be needed in a conventional measurement-based scheme to stabilize $|\phi\rangle$. Although the pure tones can be generated using microwave modulation techniques from three sources only, the tolerance to imperfections in the matching of the couplings amounts to about 10%, which can be easily achieved in superconducting qubit design. A primary virtue of our protocol is that it can be extended to larger systems because it assumes only that the system Hamiltonian can be precisely engineered (a general requirement for all quantum information implementations) and that abundant, off-the-shelf room-temperature microwave generators are available. Moreover, the protocol can take advantage of any available high-fidelity readout capability by passively monitoring the cavity outputs, enabling purification by real-time conditioning as demonstrated by our 30% reduction in state infidelity using a Josephson amplifier.

Therefore, autonomous feedback is uniquely suited to exploiting all available state-of-the-art hardware and is an ideal platform on which to construct more complicated protocols. Possible avenues for future experiments include implementing a 'compound' Bell state stabilization protocol, using a four-qubit quantum register operating two independent autonomous stabilization loops complemented by an entanglement distillation step²⁹. The quantum engineering concept implemented in our experiment could also be applied to autonomously stabilize a coherent two-state manifold of Schrödinger cat states of a superconducting cavity³⁰, thus possibly achieving a continuous version of qubit quantum error correction.

METHODS SUMMARY

Alice and Bob are single-junction 3D transmons with qubit frequencies $\omega_A^0/2\pi = 5.238$ GHz and $\omega_B^0/2\pi = 6.304$ GHz, anharmonicities $\alpha_A/2\pi = 220$ MHz and $\alpha_B/2\pi = 200$ MHz, relaxation times $T_1^A = 16$ μ s and $T_1^B = 9$ μ s, and pure dephasing times $T_\phi^A = 11$ μ s and $T_\phi^B = 36$ μ s, respectively. They are coupled to a rectangular cavity ($\omega_C^{\text{eg}}/2\pi = 7.453$ GHz) with nearly equal dispersive couplings, $\chi_A/2\pi = 6.5$ MHz and $\chi_B/2\pi = 5.9$ MHz, that are larger than the cavity linewidth, $\kappa/2\pi = 1.7$ MHz. The set-up is mounted on the base of a dilution refrigerator (Extended Data Fig. 1) and controlled using heavily attenuated and filtered microwave lines. The room-temperature microwave set-up generates all microwave drives in a manner that is insensitive to drifts in generator phases. Single-shot joint readout with fidelity of 96% was performed using a JPC (Extended Data Fig. 2). We checked, by performing tomography of Clifford states, that the measured fidelity of the Bell state was not significantly altered by systematic errors in single-qubit rotations and measurements (Extended Data Fig. 3). The choice of drive amplitudes used for Bell state stabilization was guided by Lindblad master equation simulations (Extended Data Fig. 4). These simulations also provided an error budget analysis for the steady-state infidelity suggesting that the dominant source of infidelity is the finite times T_1 and T_ϕ .

Online Content Any additional Methods, Extended Data display items and Source Data are available in the online version of the paper; references unique to these sections appear only in the online paper.

Received 18 July; accepted 22 October 2013.

Published online 24 November 2013.

- Nielsen, M. A. & Chuang, I. L. *Quantum Computation and Quantum Information* (Cambridge Univ. Press, 2004).

- Sayrin, C. *et al.* Real-time quantum feedback prepares and stabilizes photon number states. *Nature* **477**, 73–77 (2011).
- Vijay, R. *et al.* Stabilizing Rabi oscillations in a superconducting qubit using quantum feedback. *Nature* **490**, 77–80 (2012).
- Risté, D., Bultink, C. C., Lehnert, K. W. & DiCarlo, L. Feedback control of a solid-state qubit using high-fidelity projective measurement. *Phys. Rev. Lett.* **109**, 240502 (2012).
- Campagne-Ibarcq, P. *et al.* Persistent control of a superconducting qubit by stroboscopic measurement feedback. *Phys. Rev. X* **3**, 021008 (2013).
- Krauter, H. *et al.* Entanglement generated by dissipation and steady state entanglement of two macroscopic objects. *Phys. Rev. Lett.* **107**, 080503 (2011).
- Brakhane, S. *et al.* Bayesian feedback control of a two-atom spin-state in an atom-cavity system. *Phys. Rev. Lett.* **109**, 173601 (2012).
- Risté, D. *et al.* Deterministic entanglement of superconducting qubits by parity measurement and feedback. *Nature* **502**, 350–354 (2013).
- Geerlings, K. *et al.* Demonstrating a driven reset protocol for a superconducting qubit. *Phys. Rev. Lett.* **110**, 120501 (2013).
- Murch, K. W. *et al.* Cavity-assisted quantum bath engineering. *Phys. Rev. Lett.* **109**, 183602 (2012).
- Barreiro, J. T. *et al.* An open-system quantum simulator with trapped ions. *Nature* **470**, 486–491 (2011).
- Poyatos, J. F., Cirac, J. I. & Zoller, P. Quantum reservoir engineering with laser cooled trapped ions. *Phys. Rev. Lett.* **77**, 4728–4731 (1996).
- Kerckhoff, J., Nurdin, H. I., Pavlichin, D. S. & Mabuchi, H. Designing quantum memories with embedded control: photonic circuits for autonomous quantum error correction. *Phys. Rev. Lett.* **105**, 040502 (2010).
- Kastoryano, M. J., Reiter, F. & Sørensen, A. S. Dissipative preparation of entanglement in optical cavities. *Phys. Rev. Lett.* **106**, 090502 (2011).
- Sarlette, A., Raimond, J. M., Brune, M. & Rouchon, P. Stabilization of nonclassical states of the radiation field in a cavity by reservoir engineering. *Phys. Rev. Lett.* **107**, 010402 (2011).
- Lin, Y. *et al.* Dissipative production of a maximally entangled steady state of two quantum bits. *Nature* <http://dx.doi.org/10.1038/nature12801> (this issue).
- Leghtas, Z. *et al.* Stabilizing a bell state of two superconducting qubits by dissipation engineering. *Phys. Rev. A* **88**, 023849 (2013).
- Wallraff, A. *et al.* Strong coupling of a single photon to a superconducting qubit using circuit quantum electrodynamics. *Nature* **431**, 162–167 (2004).
- Schreier, J. A. *et al.* Suppressing charge noise decoherence in superconducting charge qubits. *Phys. Rev. B* **77**, 180502 (2008).
- Nigg, S. E. *et al.* Black-box superconducting circuit quantization. *Phys. Rev. Lett.* **108**, 240502 (2012).
- Schuster, D. I. *et al.* Resolving photon number states in a superconducting circuit. *Nature* **445**, 515–518 (2007).
- Lalumière, K., Gambetta, J. M. & Blais, A. Tunable joint measurements in the dispersive regime of cavity QED. *Phys. Rev. A* **81**, 040301 (2010).
- Tornberg, L. & Johansson, G. High-fidelity feedback-assisted parity measurement in circuit QED. *Phys. Rev. A* **82**, 012329 (2010).
- Paik, H. *et al.* Observation of high coherence in Josephson junction qubits measured in a three-dimensional circuit QED architecture. *Phys. Rev. Lett.* **107**, 240501 (2011).
- Filipp, S. *et al.* Two-qubit state tomography using a joint dispersive readout. *Phys. Rev. Lett.* **102**, 200402 (2009).
- Bergeal, N. *et al.* Phase-preserving amplification near the quantum limit with a Josephson ring modulator. *Nature* **465**, 64–68 (2010).
- Wooters, W. K. Entanglement of formation of an arbitrary state of two qubits. *Phys. Rev. Lett.* **80**, 2245–2248 (1998).
- Slichter, D. H. *et al.* Measurement-induced qubit state mixing in circuit QED from up-converted dephasing noise. *Phys. Rev. Lett.* **109**, 153601 (2012).
- Reichle, R. *et al.* Experimental purification of two-atom entanglement. *Nature* **443**, 838–841 (2006).
- Leghtas, Z. *et al.* Hardware-efficient autonomous quantum memory protection. *Phys. Rev. Lett.* **111**, 120501 (2013).

Acknowledgements Facility use was supported by the Yale Institute for Nanoscience and Quantum Engineering and the National Science Foundation (NSF) MRSEC DMR 1119826. This research was supported by the Office of the Director of National Intelligence (ODNI), Intelligence Advanced Research Projects Activity (IARPA) W911NF-09-1-0369, by the US Army Research Office W911NF-09-1-0514, and by the NSF DMR 1006060 and DMR 0653377. M.M. acknowledges partial support from the Agence National de la Recherche under the project EPOQ2 ANR-09-JCJC-0070. S.M.G. and Z.L. acknowledge support from the NSF DMR 1004406. All statements of fact, opinion or conclusions contained herein are those of the authors and should not be construed as representing the official views or policies of IARPA, the ODNI or the US government.

Author Contributions S.S. performed the experiment and analysed the data with assistance from M.H. and Z.L. Z.L. proposed the autonomous feedback protocol and performed numerical simulations under the guidance of M.M. K.M.S., A.N. and L.F. contributed to the experimental apparatus, and U.V. contributed to the theoretical modelling under the guidance of S.M.G. M.H.D. supervised the project. S.S., M.H. and M.H.D. wrote the manuscript. All authors provided suggestions for the experiment, discussed the results and contributed to the manuscript.

Author Information Reprints and permissions information is available at www.nature.com/reprints. The authors declare no competing financial interests. Readers are welcome to comment on the online version of the paper. Correspondence and requests for materials should be addressed to S.S. (shyam.shankar@yale.edu) or M.H.D. (michel.devoret@yale.edu).

METHODS

Qubit–cavity implementation. The two transmon qubits were fabricated with double-angle- evaporated Al/AlO_x/Al Josephson junctions, defined using the bridge-free electron-beam lithography technique^{31,32}, on double-side-polished 3 mm-by-10 mm chips of *c*-plane sapphire. They were coupled to the TE₁₀₁ mode of a rectangular copper cavity. The room-temperature junction resistances (Alice, 7.5 kΩ; Bob, 5.6 kΩ), antenna pad dimensions (Alice, 1.4 mm by 0.2 mm; Bob, 0.68 mm by 0.36 mm) and cavity dimensions (35.6 mm by 21.3 mm by 7.6 mm) were designed using finite-element simulations and black-box circuit quantization analysis²⁰ to give Alice and Bob qubit frequencies of $\omega_A^0/2\pi = 5.238$ GHz and $\omega_B^0/2\pi = 6.304$ GHz, qubit anharmonicities of $\alpha_A/2\pi = 220$ MHz and $\alpha_B/2\pi = 200$ MHz, a cavity frequency of $\omega_c^{\text{eg}}/2\pi = 7.453$ GHz, and nearly equal dispersive couplings of $\chi_A/2\pi = 6.5$ MHz and $\chi_B/2\pi = 5.9$ MHz. The cavity was coupled to input and output transmission lines with quality factors $Q_{\text{IN}} \approx 100,000$ and $Q_{\text{OUT}} = 4,500$, such that its linewidth, $\kappa/2\pi = 1.7$ MHz, was set predominantly by Q_{OUT} .

As shown in the experiment schematic (Extended Data Fig. 1), the cavity and the JPC set-up was mounted on the base stage of a cryogen-free dilution refrigerator (Oxford Triton200). As is common practice for superconducting qubit experiments, the cavity and JPC were shielded from stray magnetic fields by aluminium and cryogenic μ -metal (Amumetal A4K) shields. The input microwave lines going to the set-up were attenuated at various fridge stages and filtered using commercial 12-GHz reflective, low-pass filters and home-made, lossy Eccosorb filters. The attenuators and filters serve to protect the qubit and cavity from room-temperature thermal noise and block microwave or optical frequency signals from reaching the qubit. The output line of the fridge consisted of reflective and Eccosorb filters as well as two cryogenic isolators (Quinstar CWJ1019K) at the base to attenuate noise coming down from higher-temperature stages. In addition, a cryogenic HEMT amplifier (Low Noise Factory LNF-LNC7_10A) at the 3 K stage provided 40 dB of gain to overcome the noise added by the following room-temperature amplification stages.

Relaxation times were measured to be $T_1^A = 16$ μ s and $T_1^B = 9$ μ s, and coherence times measured with a Ramsey protocol were $T_2^A = 8$ μ s and $T_2^B = 12$ μ s, resulting in dephasing times of $T_\phi^A = 11$ μ s and $T_\phi^B = 36$ μ s. Black-box quantization analysis of the qubit–cavity system suggest that the relaxation times were limited by the Purcell effect³³. Coherence times did not improve using an echo pulse, suggesting that they were limited by thermal photons present in the fundamental and higher modes of the cavity³⁴ as well as by non-zero qubit temperature (~ 75 mK).

Control of stabilization drives. The room-temperature set-up must generate and control microwave tones in a manner such that the experiment is insensitive to drifts in the phase between microwave sources over the timescale of the experiment. Although all sources are locked to a common rubidium frequency standard (SRS FS725), they drift apart in phase on a timescale of a few minutes. Therefore, for example, the four Rabi drives on the qubits during Bell state stabilization cannot be produced by four separate sources because the phase of the drives need to be controlled precisely. The phase drift was eliminated by using one microwave source per qubit and generating the desired frequencies using single-sideband modulation (Extended Data Fig. 1). The qubit drives were produced by sources f_{Alice} and f_{Bob} (Vaunix Labbrick LMS-802), set 100 MHz below the respective zero-photon qubit frequencies. For Bell state stabilization, these tones were mixed using IQ mixers (Marki IQ4509) with 100-MHz and 82-MHz sine waves produced by a Tektronix AWG5014C arbitrary waveform generator (AWG). The mixer outputs at the desired frequencies can be expressed mathematically as $A_A^0 \cos(\omega_A^0 t + \phi_A^{\text{arb}} + \phi_A^0)$, $A_B^0 \cos(\omega_B^0 t + \phi_B^{\text{arb}} + \phi_B^0)$, $A_A^n \cos(\omega_A^n t + \phi_A^{\text{arb}} + \phi_A^n)$ and $A_B^n \cos(\omega_B^n t + \phi_B^{\text{arb}} + \phi_B^n)$. Here ϕ_A^{arb} and ϕ_B^{arb} are respectively the arbitrary phases of the microwave sources f_{Alice} and f_{Bob} , which can drift during an experiment, and ϕ_A^0 , ϕ_B^0 , ϕ_A^n and ϕ_B^n are set by the AWG as well as the length of the cables going to the qubit–cavity system, and are therefore fixed over the course of the experiment. The relationship between the drive phases required for the stabilization protocol is $\phi_A^0 - \phi_B^0 = \phi_A^n - \phi_B^n + \pi$. This is achieved in experiment by fixing ϕ_A^0 , ϕ_A^n and ϕ_B^0 and sweeping ϕ_B^n .

The cavity drives for stabilization were generated by two sources (Agilent E8267 and N5183), f_c^{eg} set to ω_c^{eg} and f_c^{ee} set to $\omega_c^{\text{ee}} = (\omega_c^{\text{eg}} - \chi_A - \chi_B)$. These drives could potentially also be produced using a single microwave source and single-sideband modulation, but this was not done because control over the phase of these drives was not important for the stabilization protocol.

Joint readout implementation with JPC. The joint readout of the qubits used for tomography was implemented with high-fidelity single-shot measurements³⁵ by pulsing the cavity input for 500 ns using the source f_c^{eg} (msmt) (Agilent N5183) set at ω_c^{eg} (Extended Data Fig. 1). The transmitted microwave pulse was directed via two circulators (Quinstar CTH1409) to the JPC amplifier, reflected with gain and then amplified at 3 K. This was followed by further signal processing at room temperature. The JPC was biased at ω_c^{eg} to provide a reflected power gain of 20 dB

in a bandwidth of 6 MHz. A noise rise of 6 dB was recorded when the amplifier was switched on, implying that 80% of the noise measured at room temperature was amplified quantum fluctuations originating from the base stage of the fridge.

The circulators also provide reverse isolation, which prevents amplified quantum fluctuations output by the JPC from impinging on the cavity and causing dephasing. In our experiment, the T_2 of the qubits was found to decrease to 3 μ s when the amplifier was turned on, suggesting that either this reverse isolation was insufficient or that the pump tone was accidentally aligned with a higher mode of the cavity. Therefore, the amplifier was turned on 100 ns before the cavity pulse was applied and turned off 1 μ s after the cavity had finished ringing down. This pulsing of the JPC ensured that the excess dephasing was absent during the stabilization period of the experiment described in the main text. Rather, it was present only during the tomography phase, when it was less important.

The output of the fridge at ω_c^{eg} had to be shifted to radio frequencies (< 500 MHz) before it could be digitized using commercial hardware. This processing was performed in a manner that was insensitive to drifts in digitizer offsets and generator phases over the timescale of the experiment. As shown in Extended Data Fig. 1, the fridge output was demodulated using an image-reject mixer (Marki IRW0618) with a local oscillator (Agilent N5183), set 50 MHz above f_c^{eg} (msmt), to produce a signal centred in frequency domain at 50 MHz. A copy of the cavity input that did not pass through the dilution refrigerator was also demodulated to give a reference copy for comparison. The signal and reference were digitized (in an Alazar ATS9870 analogue-to-digital converter) and finally digitally demodulated in the PC to give in-phase and quadrature signals ($I(t)$, $Q(t)$). This room-temperature analogue and digital signal processing ensured that the measured ($I(t)$, $Q(t)$) were insensitive to drifts in digitizer offsets and generator phases.

A 240-ns section of the cavity response after ring-up was averaged to give a measurement outcome (I_m , Q_m). Reference histograms along the I_m axis are shown in Extended Data Fig. 2a. These reference histograms were produced using qubits initialized in $|gg\rangle$, by a heralding measurement³⁶, with a fidelity of 99.5%. The histogram labelled GG was recorded using this initialized state, whereas that labelled \overline{GG} was recorded after a π -pulse on Alice. Similar \overline{GG} histograms could be produced after a π -pulse on Bob or on both qubits. The two histograms are fitted with Gaussian distributions; of the two, the GG histogram has a standard deviation that is smaller by a factor of ~ 0.75 , owing to amplifier saturation, resulting in a larger amplitude. However, the areas under each histogram are identical, as expected. The different standard deviations imply that the threshold (I_m^{th}/σ) distinguishing outcomes associated with GG from those associated with \overline{GG} cannot be set symmetrically between the two distributions. Rather, $I_m^{\text{th}}/\sigma = 5$, shifted towards GG , ensuring that the error induced by the overlap of the distributions are equal. Because the Gaussians are separated by 5.5 standard deviations, the indicated threshold would imply a readout fidelity of 99.5% calculated from the overlap of the distributions.

These well-separated Gaussian distributions indicate that the readout implements a close-to-ideal measurement of the observable $|gg\rangle\langle gg|$. However, excess counts are observed in \overline{GG} when the qubits are prepared in $|gg\rangle$, and vice versa, owing to T_1 events as well as transitions induced by the measurement tone. These errors reduce the fidelity from that calculated simply from the overlap of the two distributions. Thus, the total measurement fidelity of the observable $|gg\rangle\langle gg|$, summarized by the diagram in Extended Data Fig. 2b, is found to be 96% for the state $|gg\rangle$ and 97% for states $|ge\rangle$, $|eg\rangle$ and $|ee\rangle$.

Calibration of systematic errors in tomography. Standard two-qubit tomography is performed by applying one of a set of four single-qubit rotations (Id, $R_x(\pi)$, $R_x(\pi/2)$, $R_y(\pi/2)$) on each qubit, followed by the readout of the observable $|gg\rangle\langle gg|$ (refs 25, 37). To implement these rotations, the AWG shapes a 100-MHz sine wave with a 6σ -long Gaussian envelope with $\sigma = 12$ ns and DRAG correction^{38,39}. The outputs of the IQ mixers (Extended Data Fig. 1) are thus Gaussian pulses resonant on the zero-photon qubit transition frequencies. The resulting 16 measured observables are expressed in the Pauli basis, and the Pauli operator averages are calculated by matrix inversion. The density matrix constructed from the Pauli operator averages is then used to calculate the fidelity of the measured state to a desired target, as described in the main text.

The ability of the tomography to represent faithfully the state of the two qubits is limited by systematic errors in the readout, in single-qubit rotations and by qubit decoherence. Although these errors have been individually reduced below 1% in superconducting qubit experiments⁴⁰, they are in the few per cent range in our system owing to insufficient combined optimization. We have estimated a worst-case combined effect of these errors on the tomography by preparing the qubits in one of 36 possible two-qubit Clifford states and then performing tomography to extract the fidelity to the target state. The fidelity of the measured state to the target (Extended Data Fig. 3) varies from a maximum of 94% for the state $|-Z, -Z\rangle$, which is least susceptible to errors from relaxation and decoherence, to a minimum of 87% for the state $|+Y, +Z\rangle$, which is among the most susceptible. The

average fidelity of 90% across all 36 states is in good agreement with that expected from the aggregate of few-per-cent errors arising from readout, rotations and decoherence. This fidelity, which is substantially higher than the maximum fidelity to the Bell state we estimate in the main text, leads us to believe that systematic errors in the tomography do not significantly alter the maximum measured fidelity to $|\phi_{-}\rangle$, of 77%.

Simulation of the stabilization protocol. The stabilization protocol consists of six drives whose amplitudes need to be optimized for maximum fidelity. We now describe simulations which suggest that this is not such a daunting task because the continuous-drive protocol is robust against modest errors in the amplitudes. As described in the theory proposal¹⁷, the dynamics of the system comprising two qubits, coupled to the cavity (the reservoir) in the presence of drives, qubit decay and qubit dephasing can be simulated using the Lindblad master equation

$$\frac{d\rho(t)}{dt} = -\frac{i}{\hbar}[H(t), \rho(t)] + \kappa D[a]\rho(t) + \sum_{j=A,B} \left(\frac{1}{T_1^j} D[\sigma_-^j] \rho(t) + \frac{1}{2T_\phi^j} D[\sigma_z^j] \rho(t) \right)$$

where

$$H(t) = \left(\chi_A \frac{\sigma_z^A}{2} + \chi_B \frac{\sigma_z^B}{2} \right) a^\dagger a + 2\varepsilon_c \cos\left(\frac{\chi_A + \chi_B}{2} t\right) (a + a^\dagger) + \Omega^0 (\sigma_x^A + \sigma_x^B) + \Omega^n \left(e^{-in(\chi_A + \chi_B)t/2} (\sigma_+^A - \sigma_+^B) + \text{c.c.} \right)$$

is the Hamiltonian of the driven system in the rotating frame of the two qubits (ω_A^0, ω_B^0) and the cavity mode ($(\omega_c^{\text{gg}} + \omega_c^{\text{ee}})/2$). The qubits are considered to be perfect two-level systems rather than the anharmonic oscillators assumed in the main text, and therefore we use Pauli operators σ_z, σ_x and $\sigma_+ = \sigma_x + i\sigma_y$. The qubit dephasing rate is $1/T_\phi^{A,B} = 1/T_2^{A,B} - 1/2T_1^{A,B}$, the Lindblad super-operator is defined for any operator O as $D[O]\rho = O\rho O^\dagger - (1/2)O^\dagger O\rho - (1/2)\rho O^\dagger O$, and ε_c is the amplitude of the drive on the cavity, which is taken to equal $\kappa\sqrt{\bar{n}}/2$, where \bar{n} is the number of photons circulating in the cavity. The Lindblad equation is solved numerically for $\rho(t)$ assuming that $\rho(0) = |\text{gg}\rangle\langle\text{gg}|$. The steady-state fidelity to $|\phi_{-}\rangle$ is estimated as $\text{Tr}((|\phi_{-}\rangle\langle\phi_{-}| \otimes I_c)\rho(\infty))$. The system was empirically found to have reached a steady state at $t = 10 \mu\text{s}$, and so $\rho(\infty)$ is taken to be $\rho(10 \mu\text{s})$.

The drive amplitudes are swept in the simulation to optimize fidelity; a representative result shown in Extended Data Fig. 4 for our system characteristics indicates that a broad range of cavity drive amplitudes greater than three photons and Rabi drive amplitudes greater than $\kappa/2$ should lead to fidelities of around 70%. The dependence of the fidelity on drive amplitudes can be qualitatively understood as follows. As discussed in the main text, the two cavity drives perform a quasi-parity measurement of the state of the qubits. The parity measurement rate is $\bar{n}\kappa/2$ for $\chi_A, \chi_B \gg \kappa$, which increases with cavity drive amplitude. Thus, the fidelity is smaller at low \bar{n} owing to the slow measurement of parity compared with the error rate induced by decoherence. However, the fidelity drops at high \bar{n} owing to the unwanted dephasing between $|\phi_{-}\rangle$ and $|\phi_{+}\rangle$ induced by the mismatch between χ_A and χ_B . Next, we see that the Rabi rates required for highest fidelity increase with \bar{n} . This effect arises from a quantum Zeno-like competition⁴¹ between the parity measurement, which pins the qubits in the odd- or even-parity subspace, and the Rabi drives, which try to induce transitions between these subspaces. The ratio of the rates of these processes is the quantum Zeno parameter, which must not be too large if the photon-number-selective Rabi drives are to correct the system fast enough. For our optimal parameters, $\bar{n} = 3$ and $\Omega^0 = \Omega^n = \kappa/2$, the quantum Zeno parameter is 3, that is, not much greater than 1. In this intermediate regime, the feedback loop does not respond to errors through fully resolved discrete quantum jumps between the various states, but rather through a quasi-continuous evolution. Moreover as seen in Extended Data Fig. 4, this continuous feedback strategy is insensitive to small errors in setting the drive amplitudes, a favourable quality for the experimental realization.

In the experiment, the drive amplitudes for the cavity and zero-photon qubit transitions were pre-calibrated with Ramsey and Rabi experiments so that they

could be set to $\bar{n} = 3$ and $\Omega^0 = \kappa/2$. However, Ω^n and the phase of the n -photon Rabi drives cannot be easily calibrated; instead they were individually swept till the fidelity was maximized. As a final optimization, \bar{n} and Ω^0 were also swept; the fidelity improved by 1–2% for $\bar{n} = 3.7$ and $\Omega^0 = \kappa/2$, marginally different from the originally chosen parameters. Overall, we found that the drive amplitudes could be varied by about 20% without reducing the fidelity by more than 1%. Thus, this result as well as the good agreement for the steady-state maximum fidelity of 67% indicates that the Lindblad simulation captures most of the physics of our experiment.

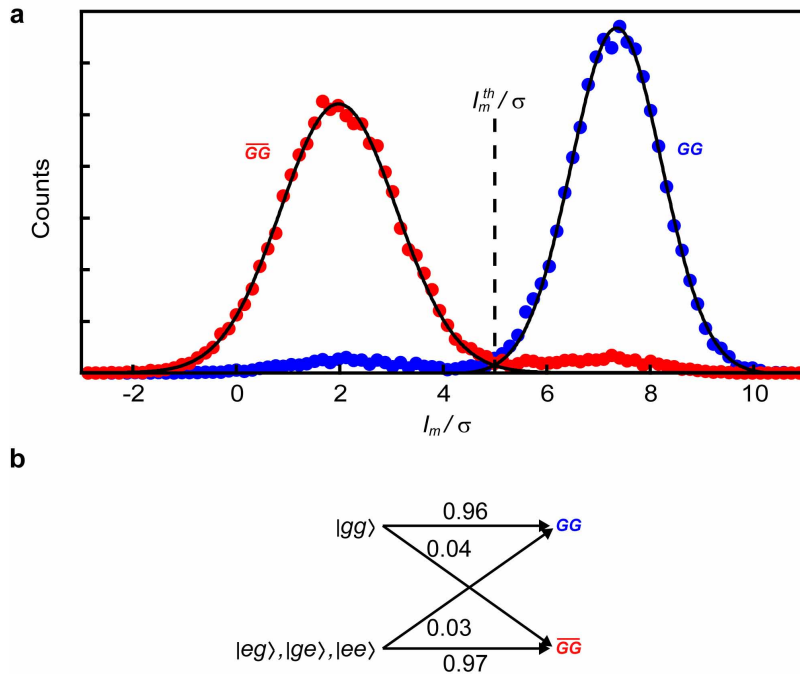
Sources of steady-state infidelity. The Lindblad simulation provides an error budget analysis for the steady-state infidelity, indicating directions for improvement. We first set $\chi_A = \chi_B = 5.9 \text{ MHz}$ and $T_1 = T_2 = \infty$, and then individually introduce the imperfections into the simulation. The ideal fidelity with drive amplitudes $\bar{n} = 3$ and $\Omega^0 = \Omega^n = \kappa/2$ is 97%, limited by the finiteness of \bar{n} . Introducing the $\sim 10\%$ χ mismatch reduces this fidelity by only 2%, indicating the robustness of the protocol to the difference between χ_A and χ_B . However, individually adding T_1 and T_ϕ processes reduces the fidelity by 12% and 8% respectively. Thus, we find that the dominant sources of infidelity are the decoherence processes inherent to the qubits and their coupling to the environment.

The T_1 values of the qubits are believed to be Purcell limited³³ (implying that κT_1 is constant) and potentially could be a factor of ten greater in the 3D cQED architecture²⁴. However, this improvement cannot be achieved by reducing κ , because that would concurrently reduce the feedback correction time and, thus, the steady-state fidelity. Instead, T_1 must be improved using a Purcell filter⁴², which results in a larger κT_1 and, thus, an overall improvement in the fidelity. Such a filter has been implemented in the 3D architecture used by our group recently and will be an immediate upgrade to the current set-up.

The current limit on T_ϕ is believed to be set by dephasing arising from thermal photons in the fundamental and higher modes of the cavity. This dephasing is given by $\kappa T_\phi \approx 1/n_{\text{th}}$, where n_{th} is the thermal occupancy of the cavity modes. The value of n_{th} calculated to give our T_2 , $n_{\text{th}} = 10^{-2}$, can be reduced by at least an order of magnitude²⁴, allowing larger κT_ϕ and, thus, an improved fidelity.

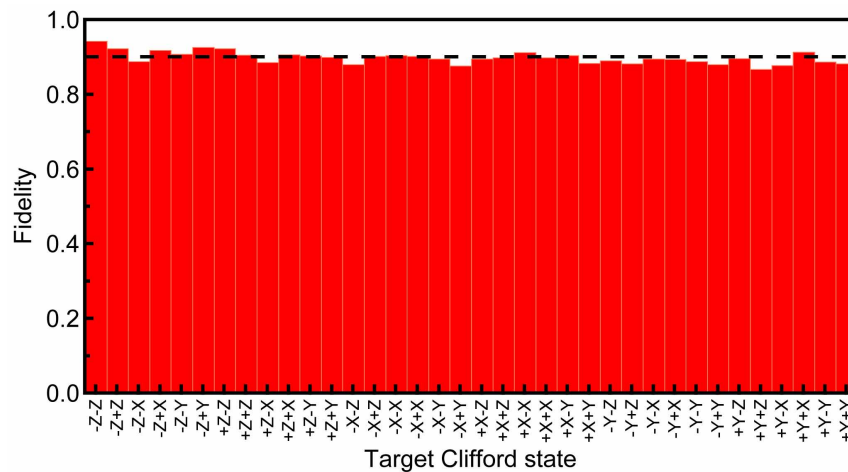
Other sources of infidelity are $\sim 4\%$ $|f\rangle$ (second excited state) population of the qubits, owing to finite temperature, as well as undesired qubit transitions that are induced by the cavity drives²⁸ which decrease T_1 . The $|f\rangle$ state population could be reduced in future experiments by additional drives on the $|e\rangle \leftrightarrow |f\rangle$ transitions. However, the T_1 reduction remains an insufficiently understood effect that requires further investigation. Nevertheless, these effects are not likely to limit the fidelity by more than 10%.

31. Lecocq, F. *et al.* Junction fabrication by shadow evaporation without a suspended bridge. *Nanotechnology* **22**, 315302 (2011).
32. Rigetti, C. *Quantum Gates for Superconducting Qubits* 174–176. PhD thesis, Yale Univ. (2009).
33. Houck, A. A. *et al.* Controlling the spontaneous emission of a superconducting transmon qubit. *Phys. Rev. Lett.* **101**, 080502 (2008).
34. Sears, A. P. *et al.* Photon shot noise dephasing in the strong-dispersive limit of circuit QED. *Phys. Rev. B* **86**, 180504 (2012).
35. Hatridge, M. *et al.* Quantum back-action of an individual variable-strength measurement. *Science* **339**, 178–181 (2013).
36. Johnson, J. E. *et al.* Heralded state preparation in a superconducting qubit. *Phys. Rev. Lett.* **109**, 050506 (2012).
37. Chow, J. M. *et al.* Detecting highly entangled states with a joint qubit readout. *Phys. Rev. A* **81**, 062325 (2010).
38. Motzoi, F., Gambetta, J. M., Reberntrost, P. & Wilhelm, F. K. Simple pulses for elimination of leakage in weakly nonlinear qubits. *Phys. Rev. Lett.* **103**, 110501 (2009).
39. Reed, M. D. *Entanglement and Quantum Error Correction with Superconducting Qubits* Ch. 5. PhD thesis, Yale Univ. (2013).
40. Devoret, M. H. & Schoelkopf, R. J. Superconducting circuits for quantum information: an outlook. *Science* **339**, 1169–1174 (2013).
41. Itano, W. M., Heinzen, D. J., Bollinger, J. J. & Wineland, D. J. Quantum Zeno effect. *Phys. Rev. A* **41**, 2295–2300 (1990).
42. Reed, M. D. *et al.* Fast reset and suppressing spontaneous emission of a superconducting qubit. *Appl. Phys. Lett.* **96**, 203110 (2010).



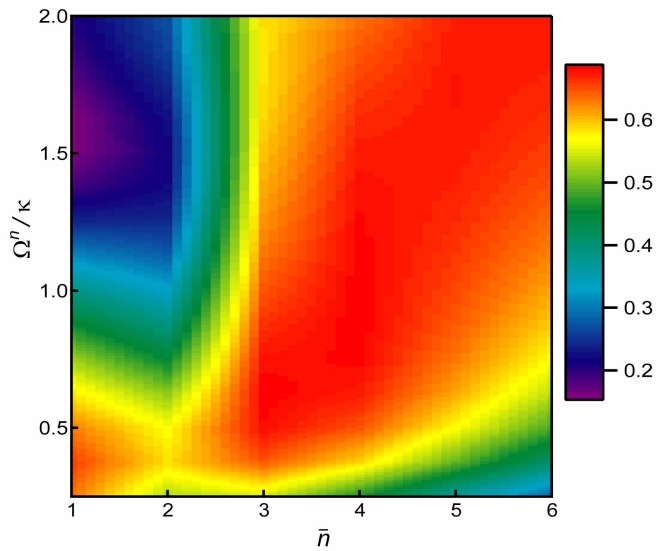
Extended Data Figure 2 | Single-shot readout of the observable $|gg\rangle\langle gg|$. **a**, Histogram of measurement outcomes recorded by the projective readout used for tomography. Outcome $I_m = 0$ implies that no microwave field was received in the I quadrature for that measurement. The GG histogram (blue dots) was recorded with the qubits initially prepared in $|gg\rangle$ with a fidelity of 99.5%. The \overline{GG} histogram (red dots) was recorded after identical preparation followed by a π -pulse on Alice. Solid lines are Gaussian fits. The horizontal

axis of measurement outcomes I_m is scaled by the average of the standard deviations of the two Gaussians, showing 5.5 standard deviations between the centres of the two distributions. Dashed line indicates the threshold that distinguishes GG from \overline{GG} : an outcome of $I_m > I_m^{\text{th}}$ is associated with GG , whereas $I_m < I_m^{\text{th}}$ is associated with \overline{GG} . **b**, Summary of the fidelity of a single projective readout of the state of the two qubits assuming the separatrix $I_m^{\text{th}}/\sigma = 5$.



Extended Data Figure 3 | Calibration of systematic errors in tomography. Fidelity of two-qubit Clifford states measured by tomography identical to that used in the Bell state stabilization protocol. Clifford states are prepared by starting in $|gg\rangle$ with a fidelity of 99.5% and then performing individual

single-qubit rotations. The fidelity varies from a maximum of 94% for the state $| -Z, -Z\rangle$, to a minimum of 87% for the state $| +Y, +Z\rangle$, averaging 90% over the 36 states (dashed line).



Extended Data Figure 4 | Predicted fidelity to $|\phi_{-}\rangle$ as a function of drive parameters \bar{n} and Ω^p under the conditions of the present experiment. Ω^0 is taken to be $\kappa/2$ in this simulation. A broad distribution of parameter values resulting in a fidelity of about 70% indicates the robustness of the autonomous feedback protocol to variations in the drives.